Materials Science & Engineering A 759 (2019) 565–573

Contents lists available at ScienceDirect

Materials Science & Engineering A

journal homepage: www.elsevier.com/locate/msea

Micromechanical response quantification using high-energy X-rays during phase transformations in additively manufactured 17-4 stainless steel

Thien Q. Phan[a], Felix H. Kim[a], Darren C. Pagan[b,*]

[a] National Institute of Standards and Technology (NIST), USA
[b] Cornell High Energy Synchrotron Source (CHESS), USA

A B S T R A C T

Recent studies of additively manufactured (AM) 17-4 stainless steel produced via laser powder bed fusion of nitrogen atomized powders have been found to contain large volume fractions of austenite (γ) compared with the fully martensitic (α′) microstructure of wrought 17-4. These AM 17-4 stainless steels have metastable microstructures that transform from a mixed phase composition to predominantly martensitic during deformation. This transformation process, combined with strong preferred crystallographic orientation (texture) that arises during building, produces complex micromechanical interactions that dictate the macroscopic response. Here, high-energy X-ray diffraction performed at a synchrotron light source is used to quantify the volume fraction of austenite and martensite, texture, and the complete orientation dependence of lattice strain (strain pole figures) at various macroscopic strains levels *in-situ* during uniaxial tension of AM 17-4. Results from wrought 17-4 are also shown for comparison. Initial martensite volume fraction of the stress-relieved AM specimen was measured to be 0.46 and increased to 0.88 after the application of a macroscopic strain of 0.03. During the transformation process, minimal crystallographic texture evolution was observed in either the γ austenite or α′ martensite. The distribution of strains in the specimen is found to be heavily influenced by both the transformation process and the initial texture. Phase transformation is found to generate tensile strains perpendicular to the applied load in untransformed γ austenite, while texture is found to produce high heterogeneity of lattice strains within lattice plane families.

1. Introduction

Additive manufacturing (AM) is recognized as a path to revolutionizing component manufacturing with benefits including: reducing wasted material, lowering costs of producing small batch parts, and printing parts with shapes and mechanical responses not possible with conventional manufacturing (e.g., machining, casting, forging) [1]. Prior to widespread adoption, technical issues associated with material quality must be addressed, such as reducing porosity and minimizing residual stresses that form during the rapid heating and cooling cycles of a build. Another pressing challenge is the need to develop understanding of the mechanical responses of the unique microstructures created in the extreme processing environments inherent to the additive manufacturing process. The example that will be explored in this paper is 17-4 stainless steel. This steel is widely used in the aerospace, petroleum, and chemical processing industries for applications requiring corrosion resistance at elevated temperatures and high-strength [2,3]. 17-4 stainless steel is a martensitic steel alloy in the wrought form, but has been shown to retain large amounts of austenite when additively manufactured from nitrogen atomized powders and exhibit strong preferred crystallographic orientation (texture) from the build process [4–6]. These previous studies have identified complex interactions between the phases that are further complicated by the strong texture. Due to the complexities of the microstructure, AM 17-4 stainless steel is well-suited to be studied by high-energy X-ray techniques, capable of quantifying the full deformation anisotropy across different families of crystal orientations. Specifically, in this work we will be presenting strain pole figure results measured during *in-situ* uniaxial tension, showing the complete anisotropy of mechanical response of different families of lattice planes from both the martensitic and austenitic phases present. The thousands of lattice strain measurements per strain pole figure enable the separation of effects of texture and phase interactions on strain partitioning in additively manufactured 17-4 stainless steel.

The starting powder feedstock used in the laser powder bed fusion (LPBF) process is manufactured via gas atomization. Traditionally, the gas used for the atomization process is chosen based on its reactivity as well as cost. The most commonly used gases for atomization are nitrogen and argon [7]. Nitrogen's primary benefit is the associated cost as it is significantly less expensive than argon. However, since nitrogen is relatively easily dissolved into metals, starting feedstocks generally have high nitrogen content. Studies have shown that higher nitrogen content in the starting feedstock powder is responsible for the retained austenite observed in as-built microstructures [4,8]. In contrast, retained austenite in as-built components is minimized using argon atomized powder. However, components built using argon atomized

* Corresponding author.
E-mail address: dcp99@cornell.edu (D.C. Pagan).

https://doi.org/10.1016/j.msea.2019.05.017
Received 30 January 2019; Received in revised form 4 May 2019; Accepted 6 May 2019
Available online 10 May 2019
0921-5093/

powders tend to exhibit much higher porosity due to the lower solubility of argon compared to nitrogen [9,10].

In this work, we study 17-4 built from powder feedstock atomized in nitrogen gas that initially contains a relatively large volume of retained austenite. In the past, numerous potential hypotheses have been put forward in the literature to explain the retained austenite [4,11–13]: strain at high angle grain boundaries, the relatively larger dislocation density, the supersaturation of austenite with phase stabilizing elements, smaller grain sizes and inter-dendritic spacing, and powder composition and manufacturing environments. Out of these, the powder composition (nitrogen content) is believed to have the greatest effect due to nitrogen's ability to lower the martensitic start temperature [8]. Critically beyond initial microstructure, nitrogen may play a large role in deformation behavior. A previous study by Biggs [14] investigated the influence of nitrogen on the martensite formation of Cr-Mn-Ni stainless steels during deformation. There, alloys that had more than 0.1 wt% nitrogen would exhibit fully austenitic microstructures, and alloys that had below 0.2 wt% nitrogen are metastable and undergo a transformation from austenite to martensite during deformation. The authors suggested that increased nitrogen content causes an increase in stacking fault energy which inhibits the nucleation of martensite, so even small variations in nitrogen content result in significant variations in microstructure and dependent mechanical properties.

At the microscale, the mechanical response of individual crystals in alloys such as AM 17-4 are expected to show significant heterogeneity due to the strong dependencies of both elastic and plastic constitutive relationships on crystal orientation and phase composition. Therefore, in order to understand the micromechanical response, the probe must be able to determine the response of different subsets of crystals to isolate those that are carrying high loads or experiencing localization of deformation that can cause premature failure. Diffraction methods have long been exploited to make this possible in metallic alloys [15] as different phase compositions and crystallographic orientation naturally diffract to different regions of real space. However, synchrotron X-ray sources combined with large panel area detectors are now facilitating the ability to probe the strain states of *all* lattice orientations present within a volume in relatively short amounts of time (minutes). With the complete orientation dependence of response determined, new insight can be gathered regarding load partitioning in complex microstructures [16,17] such as those generated during the additive manufacturing process. In addition, it greatly reduces the possibility of 'missing' the subset of grains that may be the most problematic due to insufficient sampling of orientation or phase space.

Herein, we assess the *in-situ* microstructural evolution and micromechanical response of AM 17-4 stainless steel built via LBPF with nitrogen atomized feedstock. Results from wrought 17-4 are presented for comparison. High-energy X-ray measurements are performed *in-situ* as the specimens are deformed in uniaxial tension. The structure of the paper is as follows. Experimental and data processing methods are described in §2.1 and §2.2, while the test materials are described in §2.3. The microstructural and micromechanical evolutions during uniaxial loading of the AM and wrought specimens 17-4 specimens are presented in §3. Lastly, the results are discussed in §4.

2. Methods and material

2.1. Experiment description

The mechanical loading and *in-situ* X-ray experiments were performed at the F2 station of the Cornell High Energy Synchrotron Source (CHESS). Specimens of 17-4 stainless steel in the stress-relieved AM and wrought conditions were deformed in uniaxial tension as diffraction and tomography measurements were performed. Computed tomography measurements were performed to determine the initial porosity of the specimens and monitor any evolution of the porosity in the AM

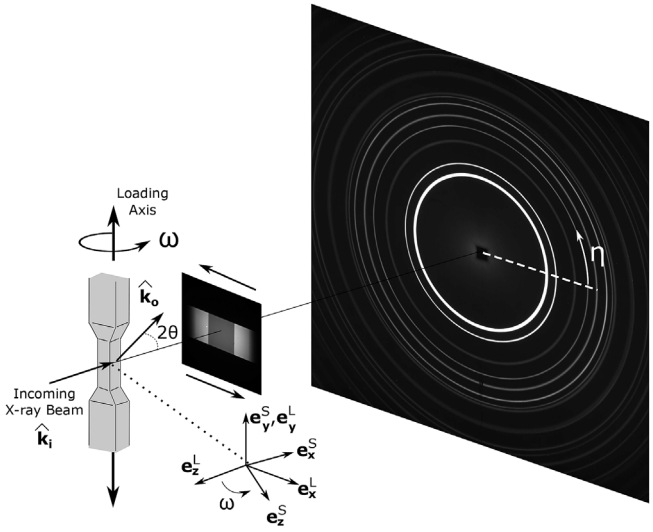

Fig. 1. Schematic of the experimental geometry employed in this work with the laboratory and sample coordinate systems denoted with L and S respectively. Incoming X-rays travel in the $\hat{k}_i$ direction and diffracted X-rays travel along $\hat{k}_o$. Measured diffracted intensity is parameterized by three angles 2θ, η, and ω. Radiographs are measured on a scintillator placed close to the specimen that can be moved out of the path of the X-ray beam and diffracted X-rays are measured on a large area detector behind the specimen.

specimen during loading. Diffraction measurements were performed to quantify the evolution of volume fraction of separate phases, crystallographic texture, and the distribution of strains within the specimen. The specimen loading and rotation with respect to the X-ray beam were performed using the second iteration of the Rotation and Axial Motion System (RAMS) load frame [18]. The load frame has a set of rotation stages within the load path which allows specimens to be rotated 360° without impeding incoming or outgoing X-rays. The tensile specimens had an 8 mm gauge length and a 1 mm × 1 mm cross section. To complete the X-ray measurements at a fixed material state, the mechanical loading was paused and the applied load was reduced to 75% of the maximum load to prevent creep. At each load step, three 1 mm tall volumes were probed along the gauge length. However, the differences in the initial texture and mechanical response of these volumes were found to be negligible (as expected from a uniform gauge) so results will focus on the center volume.

A schematic of the experimental geometry is shown in Fig. 1. The laboratory and sample coordinate systems are denoted with the superscripts L and S respectively. The laboratory coordinate system is defined such that the incoming beam direction $\hat{k}_i$ is equal to $-\boldsymbol{e}_z^L$ and the rotation/load axis of the specimen lies parallel to $\boldsymbol{e}_y^L$. The energy of the incoming X-ray beam was 61.332 keV (wavelength $\lambda = 0.0202$ nm) and was 2 mm wide (along $\boldsymbol{e}_x^L$) and 1 mm tall (along $\boldsymbol{e}_y^L$). The beam was made sufficiently wide to illuminate the entire cross section of the specimen as it rotated. Diffracted X-rays were parameterized by three angles: twice the Bragg angle, 2θ, measured as the angle between incoming and diffracted X-rays ($\angle \boldsymbol{k}_i, \boldsymbol{k}_o$), the azimuthal angle, η, measured from horizontal on the area detector, and ω, the current specimen rotation angle when measurements are made. We note that the sample and laboratory coordinate systems are in coincidence when $\omega = 0$.

Tomography and diffraction measurements were performed sequentially at each load step. The tomography measurements were made using a translating detector system that can move in and out of the path of the transmitted X-ray beam, sitting approximately 10 mm behind the specimen. The detection system consists of a Retiga 4000DC[1] optical camera focused onto a LuAg:Ce scintillator with a 5 × lens. The camera had 2048 pixels × 2048 pixels and the effective pixel size was 1.48 μm. The scintillator was located 8 mm behind the specimen. At each load step 3600 radiographs were taken over a 360° range (0.1° spacing) with

exposure times of 1.25 s. Once the radiographs were collected, the detector assembly was moved out of the way and powder diffraction images were collected on a GE 41RT+[1] area detector. The detector had 2048 pixels × 2048 pixels and a 200 μm pixel size. This detector was located 807 mm behind the specimen. To collect full pole figures, diffraction images were collected in 36 increments over 180° (5° spacing) as the specimen continuously rotated in ω. The integration time for each rotation segment was 1 s. The geometry of the diffraction experiment was determined using a CeO_2 powder diffraction standard (National Institute of Standards and Technology 674B).

The macroscopic engineering stress-strain responses of the AM and wrought specimens are shown in Fig. 2. Macroscopic stress was determined from the specimen cross section and a load cell placed in the load path above the specimen. The macroscopic strain was determined from digital image correlation (DIC) analysis of the specimen surface using an optical camera placed to the side of the specimen. The DIC analysis to determine macroscopic strain values was performed using a custom set of Matlab[1] scripts. Each individual marker in Fig. 2 corresponds to a point where strain measurements were made using DIC. The AM specimen was deformed to a final strain of 0.03 while the wrought specimen was deformed only to 0.02 due to time constraints.

2.2. Data processing

The process for building the pole figures (including strain pole figures) is outlined in Fig. 3 from the powder diffraction images. Background diffraction theory is included in an appendix. The Debye rings taken at a given ω value are divided into 72, 5° azimuthal bins. The azimuthal bins are then integrated using routines from the HEXRD software package to generated one-dimensional (1-D) line profiles [19]. All peaks in the 1-D line profiles are then fit simultaneously using Pseudo-Voigt analytic functions. From the fit peak data, the intensity of each peak and the centroid 2θ values are calculated. The intensity data is used to calculate the probability of finding lattice planes of a given orientation for the orientation pole figure and the 2θ values are used to calculate strain. As the last step, measured scalar values for each peak in an azimuthal bin are then mapped to a sample direction on the unit sphere. The mapping from diffraction angles to a direction in the sample frame $\hat{\boldsymbol{q}}^S$ in the experimental geometry shown in Fig. 1 is [19]:

$$[\hat{\boldsymbol{q}}^S] = \frac{d_{hkl}}{\lambda}\begin{bmatrix}\cos(\omega) & 0 & -\sin(\omega)\\ 0 & 1 & 0\\ \sin(\omega) & 0 & \cos(\omega)\end{bmatrix}\begin{bmatrix}\sin(2\theta)\cos(\eta)\\ \sin(2\theta)\sin(\eta)\\ -\cos(2\theta)-1\end{bmatrix} \tag{1}$$

where d_{hkl} is the spacing of a set of lattice planes.

The inversion of orientation pole figure data to calculate orientation distribution functions (ODFs) was performed using the ODFPF software package and a procedure detailed in Ref. [20]. The package uses finite elements to represent functions over pole figures and orientation space (specifically Rodrigues space). The first step consists of optimizing nodal values on spherical meshes representing the pole figures to best match the discrete intensity measurements. The nodal values are then normalized such that the pole figures integrate to 4π. A system matrix $[M]$ is then generated which relates nodal values of the pole figure data to nodal values of the ODF, A:

$$\{P_{hkl}\} = [M]\{A\} \tag{2}$$

where {} indicates the nodal values of the respective functions. The rows of the system matrix correspond to weights to evaluate path integrals through orientation space equivalent to the fundamental relationship between orientation pole figures (P_{hkl}) and orientation distribution functions

[1] Mention of commercial products does not imply endorsement by the National Institute of Standards and Technology, nor does it imply that such products or services are necessarily the best available for the purpose.

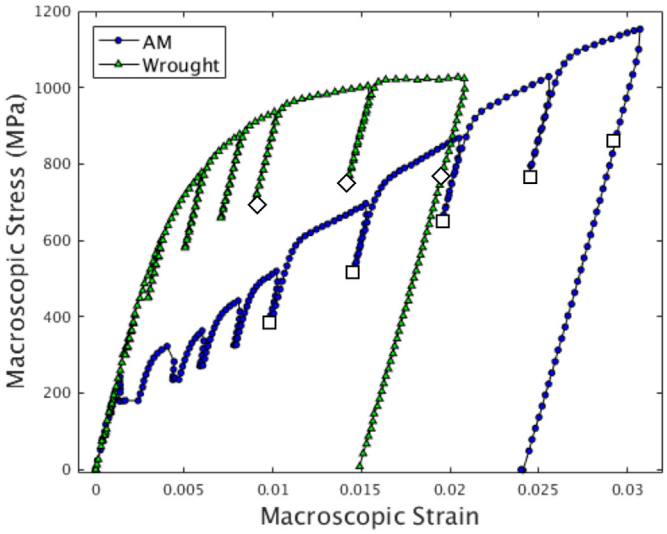

Fig. 2. Macroscopic stress-strain measurements of the additively manufactured and wrought 17-4 stainless steel specimens. Unload segments of the macroscopic response correspond to where diffraction measurements were made. Square and diamond glyphs correspond to strain pole figure measurements shown in Figs. 7–9.

$$P_{hkl}(\hat{q}) = \frac{1}{2\pi}\oint_{\pm \boldsymbol{n_{hkl}}\parallel\hat{\boldsymbol{q}}} A\,\mathrm{d}\phi. \tag{3}$$

The orientations spanned by each path integral are all orientations which transform lattice plane normals in the crystal frame to sample directions. The final step to determine an ODF is to optimize the nodal values of the ODF $\{A\}$ to minimize the residual between P_{hkl} and $[M]\{A\}$. For this work, the pole figure meshes had 14402 nodes, while the ODF meshes had 3935 nodes.

Micro-computed tomography (μCT) reconstructions were generated using the TomoPY software package [21]. The Gridrec algorithm was used to perform the reconstruction. The μCT reconstructions have a voxel size of $(1.48\,\mu m)^3$. The μCT analysis was performed in the environment of VG Studio Max 3.1[1] [22]. Features (pores) reconstructed in slices of the initial and final states were manually compared to find the corresponding volumes. The volume in the initial state had 544 reconstructed slices and the final state had 561 slices, consistent with the final macroscopic strain of 0.03. An adaptive Gaussian filter (smoothing: 5, edge threshold: 0.1) was used to filter the reconstructions, and a local thresholding technique, VGEasyPore[1], was used to threshold the reconstructions. The local contrast threshold was found based on the noise level of the reconstructions [23].

DIC strain fields for the AM and wrought specimens at maximum macroscopic strains (0.03 for AM, 0.02 for wrought) were generated using Correlated Solutions Vic2D[1] software with a subpixel size of 21 and a step size of 5. A pseudo noise analysis was performed using a subset of five images taken as the specimen was unloaded. The 1-standard deviation noise level of strains for the AM and wrought strain fields was found to be approximately 3.5×10^{-4}. Here, we consider variations in the strain fields higher than three times this standard deviation (± 0.001) to be valid and not an artifact of the DIC processing [24]. However, additional factors not considered here, such as consistency in lighting, may add to the total DIC strain uncertainty.

2.3. Material

The 17-4 stainless steel test specimens were produced at the National Institute of Standards and Technology (NIST) using laser powder bed fusion in an EOSINT M 270 system[1] following the manufacturer's nominal build conditions. The laser power and velocity were

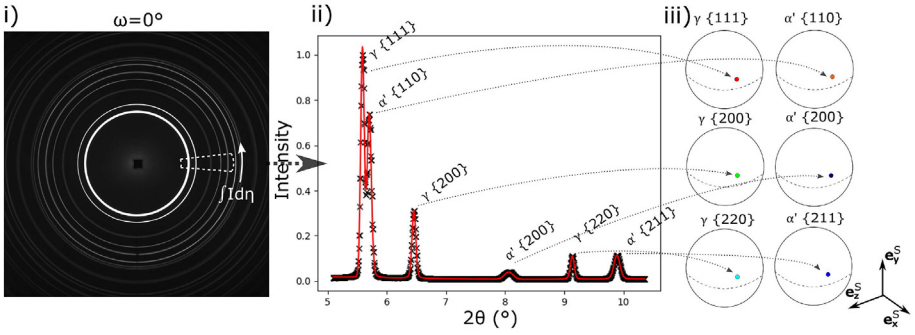

Fig. 3. Diagram of the pole figure generation process. i) Raw diffraction images are binned into 5° azimuthal bins. ii) Diffraction peaks in each, now, 1-D spectrum are fit to find intensity and lattice plane spacing from which orientation probability and strain are determined. iii) Values corresponding to a specific 2θ, η, and ω triplet are mapped to the unit sphere.

195 W and 1000 mm/s, respectively. The build layers were 20 μm thick and the laser moved in a checkerboard scanning pattern with rotation between layers. Hatch distance between laser scan tracks was 100 μm. The feedstock was a nitrogen atomized powder supplied by the system manufacturer, similar to those used in previous studies at NIST [3,25]. A separate manuscript summarizes relevant powder parameters [26]. Chemical composition measurements performed by a third-party laboratory on nitrogen atomized 17-4 powder feedstocks (virgin and recycled) and the solid AM built part all show virtually identical nitrogen content of 0.16 wt%, 0.16 wt%, and 0.15 wt% respectively. The AM process does not change the nitrogen content from the powder to the solid part.

An AM block measuring 50 mm × 150 mm × 8 mm (width × length × height) was deposited directly on a build plate. The block and build plate were stress-relief heat treated at 650° C for 1 h according to the manufacturer's recommendation. The block was then removed from the build plate via electric discharge machining (EDM). Uniaxial tension specimens were then machined from the block using EDM. The specimen was cut from the build plate such that the build direction (BD) was along $\boldsymbol{e}_z^S$ perpendicular to the loading direction. Following the material processing, this specimen will be labeled 'AM-SR'.

For comparison to the AM-SR specimen, a second specimen was cut from a wrought 17-4 stainless steel plate. The plate was hot rolled and annealed. The specimens were cut from the plates such that $\boldsymbol{e}_x^S$ was along the transverse direction (TD), $\boldsymbol{e}_y^S$ was along the normal direction (ND), and $\boldsymbol{e}_z^S$ was along the rolling direction (RD). The specimen cut from this wrought plate will be labeled 'W'.

Microstructure analysis via optical microscopy, scanning electron microscopy, laboratory-based X-ray diffraction, and energy dispersive X-ray spectroscopy were previously performed by Cheruvathur et al. [3] on similar 17-4 samples built using the same machine at NIST using the same build parameters. The as-built AM parts exhibited dendritic/cellular microstructures, with microsegregation of Fe, Cr, and Nb along the dendrite boundaries. After the stress-relief heat treatment, very little changed in the dendritic solidification microstructure and a small reduction of austenite volume fraction was observed.

Characterization was conducted using X-ray data collected from the specimens prior to loading. From the initial computed tomography reconstructions and using the process described in §2.1, the initial pore volume fraction in the AM-SR specimen was found to be 1.71×10^{-4} with 125 distinct pores identified. The porosity in the W specimen was negligible as expected and not tracked further in the experiment. These porosity measurements are a lower bound, as the minimum feature size that can be resolved is 8 voxels (3.24 μm^3) based on the Nyquist sampling theorem [27], and the volume of the smallest pore detected was 10 voxels. The low porosity in the AM-SR specimen was assumed not to be an influence in the partitioning of strain in the data analysis. The volume fraction of retained austenite in the AM-SR specimen was calculated by integrating all diffracted intensity from the γ austenite {111} and α′ martensite {110} lattice planes across all sample directions, and then normalizing the intensities by the unit cell structure factor, unit cell volume, multiplicity, and polarization factor [28]. The initial volume fraction of γ austenite was found to be 0.54 and the α′ martensite was 0.46. The initial lattice parameters of the AM-SR specimen were found to be 0.2934 nm for the martensite phase and 0.3523 nm for the austenite phase, while the lattice parameter of the austenite phase in the W specimen was found to be 0.3520 nm. The large diffraction volume and instrument resolution precluded determination of the tetragonality of martensite phase in the AM-SR specimen, but tetragonality is expected to be minimal due to the low carbon content of the material (< 0.05 wt%).

The textures of the two specimens were also characterized from the diffraction data. Fig. 4 shows the initial ODFs and orientation pole figures from the γ austenite of the AM-SR specimen (Fig. 4A), α′ martensite of the AM-SR specimen (Fig. 4B), and α′ martensite of the W specimen (Fig. 4C). The ODFs are expressed in the cubic fundamental region of Rodrigues space and ODF values are expressed in terms of multiples of uniform distribution (MUD). All three ODFs show fiber textures: < 110 > along $\boldsymbol{e}_z^S$ (transverse to loading) in both the γ austenite of the AM-SR specimen and α′ martensite of the W specimen, while the α′ martensite of the AM-SR specimen has < 100 > along $\boldsymbol{e}_z^S$. However, both of the martensite textures are not very strong. The fiber textures can be discerned from the straight lines across the ODF, since

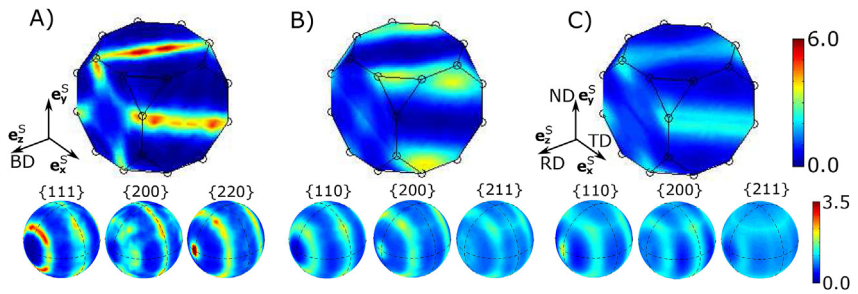

Fig. 4. Initial ODFs of the (A) γ austenite of the AM-SR specimen, (B) α′ martensite of the AM-SR specimen, and (C) α′ martensite of the W specimen expressed over the cubic fundamental region in Rodrigues space along with the measured orientation pole figures from which the ODF was generated. The ODFs are expressed in terms of multiples of uniform distribution (MUD).

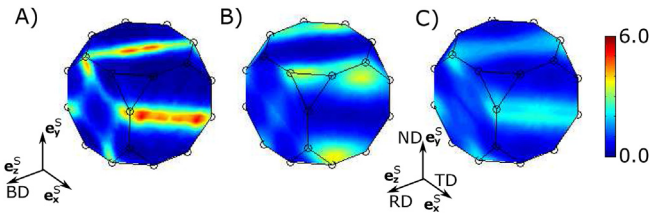

Fig. 5. Finals ODFs of the (A) γ austenite of the AM-SR specimen, (B) α′ martensite of the AM-SR specimen, and (C) α′ martensite of the W specimen expressed over the cubic fundamental region in Rodrigues space. The ODFs are expressed in terms of multiples of uniform distribution (MUD).

families of crystallographic orientations related by a single axis (in this case the fiber axis) are straight lines in Rodrigues space [29]. The {111} planes in the γ austenite and {110} planes in the α′ martensite of the AM-SR specimen are aligned with build direction, suggesting preferred orientations developing during solidification. The similarities between these pole figures indicate that these planes serve as interfaces between the γ austenite and α′ martensite which is expected from the martensitic relationship in steel [30]. As seen in Fig. 4C, we also see that the {110} planes are preferentially aligned with the rolling direction, which is consistent with rolling of most body centered cubic (BCC) metals [31].

3. Results

3.1. Microstructure evolution

As described in §2.1, the microstructures of the specimens were tracked throughout the mechanical loading using multiple X-ray techniques. The lower bound porosity of the AM-SR specimen at the end of the test was found to have slightly risen to 1.78×10^{-4} (a 5% increase) and no new pores were determined to have nucleated. There was also minimal evolution of the texture in the two specimens. Fig. 5 shows the final textures of (Fig. 5A) the γ austenite of the AM-SR specimen, (Fig. 5B) the α′ martensite of the AM-SR specimen, and (Fig. 5C) the α′ martensite of the W specimen. In Fig. 5A, there is a slight decrease in texture strength on the surface perpendicular to $\boldsymbol{e}_y^S$ and a slight increase on the surface perpendicular to $\boldsymbol{e}_x^S$. There is minor decrease in texture strength observed in the α′ martensite in AM-SR that can be seen in Fig. 5B. No texture evolution can be observed in α′ martensite of the W specimen in Fig. 5C.

The most prominent microstructural change that occurred during the test was the transformation of a large portion of the retained γ austenite to α′ martensite in the AM-SR specimen. Fig. 6 shows the evolution of the relative volume fractions of the phases with respect to applied macroscopic strain. The inset shows the uncertainties of the volume fraction measurements. Uncertainties were estimated from the standard deviation of 1000 trials where each intensity measurement on a pole figure had random noise applied with a standard deviation of 1% of the intensity maximum. Once plastic deformation began, the volume fraction of the α′ martensite monotonically increased with applied load (from 0.46 to 0.88). The transformation of γ austenite to α′ martensite without appreciable texture change will be discussed later.

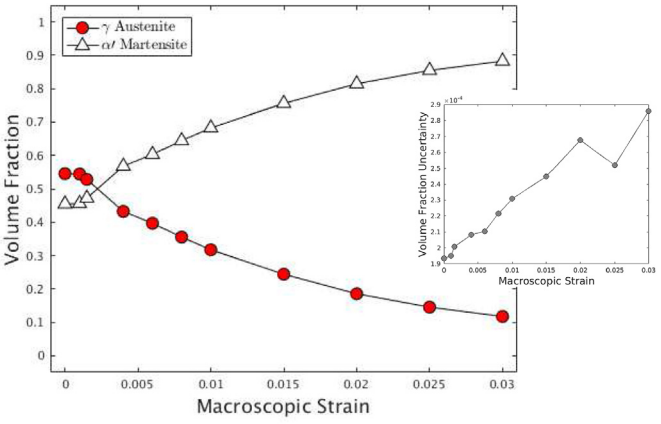

Fig. 6. Evolution of the volume fractions of γ austenite and α′ martensite in the AM-SR specimen versus macroscopic strain applied. Inset: Uncertainty associated with each volume fraction measurement.

3.2. Evolution of strain partitioning

The evolution of the strain pole figures measured from the AM-SR and W specimens are presented in Figs. 7–9. These results focus on the evolution at applied macroscopic strains of 0.01 and beyond. The points at which the strain pole figures were measured with respect to the macroscopic response can be viewed in Fig. 2. To aid interpretation of the lattice strain data, the corresponding orientation pole figures are shown to the side. For interpreting the strain pole figures, strains along the loading direction ($\boldsymbol{e}_y^S$) will generally be positive (in tension), while strains in the plane normal to the loading direction ($\boldsymbol{e}_x^S - \boldsymbol{e}_z^S$) are generally expected to be negative due to Poisson contraction. The error of lattice strain measurements at the CHESS facility have been determined to be 10^{-4} [32,33].

When comparing the strains between the γ austenite and α′ martensite in the AM-SR specimen in Figs. 7 and 8, we see that the maximum strains in the α′ martensite are significantly higher then the γ austenite. In both phases, strains are highest for the {*h*00} family lattice planes, consistent with the [100] crystallographic direction generally being the most compliant in cubic crystals [34]. In some sets of lattice planes there is significant heterogeneity of strains in the $\boldsymbol{e}_x^S - \boldsymbol{e}_z^S$ plane. In an untextured, single phase material, these strains would be expected to be radially symmetric about $\boldsymbol{e}_y^S$. In the {111} planes of the γ austenite, the most negative strains are in the build direction. Also of note is that the strains in the {200} lattice planes in the $\boldsymbol{e}_x^S - \boldsymbol{e}_z^S$ plane are completely in tension, instead of the expected contraction.

To contrast, lattice strains in the α′ martensite of the W specimen are significantly lower than those in the AM-SR specimen at comparable load levels (see Fig. 9, 0.020 applied strain versus Fig. 8, 0.025 applied strain). Differences between the W and AM-SR α′ martensite strain magnitudes can most likely be attributed to differences in strain partitioning due to the presence of γ austenite in the AM-SR specimen. In the W specimen, heterogeneity of contraction in the $\boldsymbol{e}_x^S - \boldsymbol{e}_z^S$ plane is also observed in the {200} pole figure and will be discussed.

4. Discussion

Rapid diffraction measurements made possible by the large fluxes of high-energy X-rays available at synchrotron sources are enabling in-depth characterization of the evolution of microstructure and micro-mechanical state *in-situ* during the deformation of engineering alloys. These new capabilities are extremely valuable for beginning to understand the mechanical interactions that occur in the complex microstructures produced during the additive manufacturing process. Herein, we demonstrated this through use of high-energy X-ray techniques in a transmission geometry to monitor the evolution of porosity, phase composition, crystallographic texture, and the complete orientation dependence of lattice strains in additively manufactured 17-4 stainless steel.

4.1. Analysis of microstructural evolution

During the uniaxial deformation of the AM-SR specimen, significant deformation induced phase transformation was measured from the respective decreases and increases of diffracted intensity from the γ austenite and α′ martensite. As the macroscopic strain applied was increased to a maximum of 0.03, the volume fraction of α′ martensite

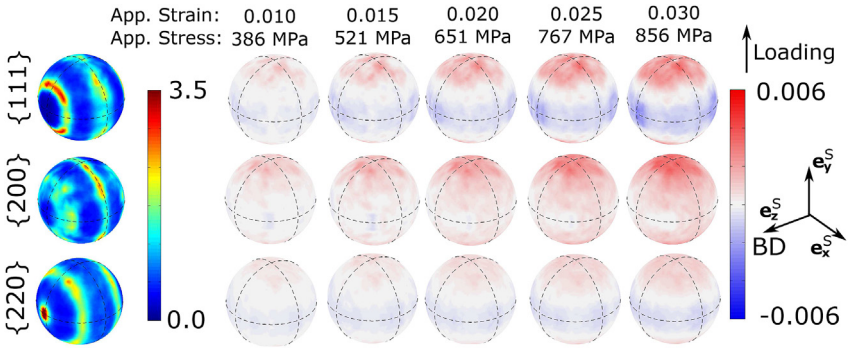

Fig. 7. Evolution of strain pole figures from the {111}, {200}, and {220} lattice planes of the γ austenite of the AM-SR specimen. Orientation pole figures from the same lattice planes are included for reference.

increased from 0.46 to 0.88. A relatively low macroscopic strain when martensite transformation occurs, similar to deformation behavior observed in this work, has been correlated to low carbon content in the austenite [35]. This early transformation behavior has been previously observed in AM 17-4 [5,6], but the effects of the phase transformation on texture evolution has not been as deeply examined. In other metastable austenitic steels, the transformation to martensite is usually accompanied by evolution of the crystallographic texture of the martensite [36,37], but in the AM-SR specimen studied in this work, very little texture evolution was observed. The < 100 > fiber texture in the α' martensite was still present and no new texture components appeared even after significant amounts of phase transformation (Figs. 4B and 5B). This lack of new texture components suggests that there was no nucleation of new martensite regions. Rather, the transformation process consisted of growth of existing martensite regions that were created during the build and heat treatment process and these existing martensite regions were likely favorably oriented variants [38]. Further microscopy is required to determine if any microstructural features (precipitates) introduced either in the gas atomization or build process are inhibiting the nucleation of martensite during deformation. Although as mentioned previously, nitrogen has been proposed as an inhibitor of the martensite nucleation process [8,14].

4.2. Analysis of mechanical response

The macroscopic stress-strain curve of the AM-SR specimen is sigmoidal in nature (Fig. 2), as opposed to the more gradual elastic plastic transition in the W specimen. In the AM-SR specimen, the initial yield stress is approximately 300 MPa, beginning with an initial region of lower hardening rate until a macroscopic strain of 0.01. Then, a region of higher hardening rate is observed from 0.01 to 0.03 when the test was completed. The hardening is attributed to the formation of deformation-induced martensite. Fig. 6 indicates that the volume fraction of martensite increases throughout the test, with a decrease in

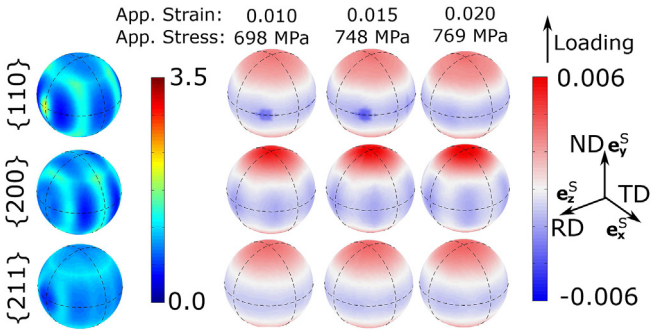

Fig. 9. Evolution of strain pole figures from the {110}, {200}, and {211} lattice planes of the α' martensite of the W specimen. Orientation pole figures from the same lattice planes are included for reference.

transformation rate with higher levels of strains. As more volume fraction of the material transforms from austenite to the stronger martensite, increasing amounts of the applied load is transferred to the martensite [39] and the yield stress increases. The sigmoidal stress-strain behavior is often seen in TRansformation Induced Plasticity (TRIP) steels [40]. However, in contrast to TRIP steels, the AM-SR specimen starts transforming almost immediately after plastic deformation begins (≈0.001 macroscopic strain). Compared with macroscopic responses of AM 17-4 presented in previous works [4,5], the shapes of the stress-strain curves are similar, but the AM-SR specimen tested here exhibited a much faster hardening rate. This difference is most likely caused by variation in applied strain rates, loading path differences from the intermittent unloads, and small variation in the starting powder feedstock.

Fig. 10 shows the 2-dimensional (2-D) fields of strain along the loading direction ε_{yy} for the AM-SR and W specimens at maximum macroscopic strain of 0.03 and 0.02, respectively. The AM-SR specimen

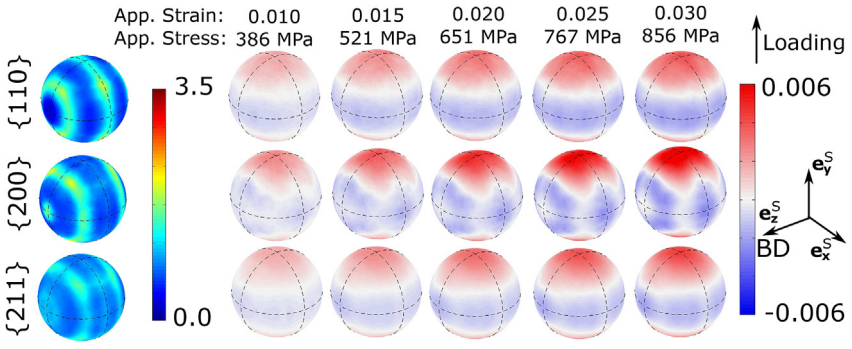

Fig. 8. Evolution of strain pole figures from the {110}, {200}, and {211} lattice planes of the α' martensite of the AM-SR specimen. Orientation pole figures from the same lattice planes are included for reference.

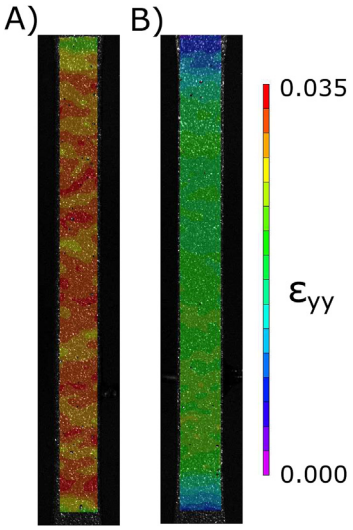

Fig. 10. A) Distribution of ε_{yy} on the specimen surface of the AM-SR specimen. B) Distribution of ε_{yy} on the specimen surface of the W specimen.

shows more heterogeneity in the strain field, with variations of approximately 0.007 over length scales of hundreds of micrometers. The W specimen deforms in a more homogenous manner, with local strain variations of approximately 0.003. Unlike other tensile tests performed on larger AM samples to failure [25], no Lüders band developed in the AM-SR specimen. Nevertheless, deformation heterogeneity is higher in the AM-SR specimen compared with the W specimen and may be due to microstructure heterogeneities created by individual laser tracks and build layers.

General trends of elastic strain partitioning between the austenite and martensite are consistent with previous studies [39]. If the directional stiffnesses of the austenite and martensite are assumed to be comparable, stresses in the loading direction in the α′ martensite are roughly double those found in the γ austenite due to the higher strength of the martensite phase. As mentioned in §3, the strains perpendicular to the loading direction measured in the AM-SR specimen are more positive than expected from Poisson contraction. In the case of the {200} lattice planes of γ austenite, the strains were even found to be tensile. According to the Bain martensite transformation model [30], an elongated unit cell of the (martensite) BCC structure can be identified within two (austenite) face centered cubic (FCC) unit cells. During transformation, this elongated unit cell transforms to the BCC structure. For discussion purposes, we will refer to this elongated unit cell as the transformation pair. The FCC and BCC crystal structures both exhibit cubic symmetry. However, the transformation pair exhibits tetragonal symmetry. The c-axis of the transformation pair corresponds to the γ and α′ [001]. The transformation consists of extension of two γ < 110 > directions (≈12% expansion) and contraction of a perpendicular [001] direction (c-axis) (≈20% contraction) [30]. Thus, the favorable orientations for transformation suggest the alignment of the c-axis with the macroscopic compressive orientations, or near that of the transverse directions during tensile loading. The only unfavorable orientations would be when the c-axis of the tetragonal pair aligns near the loading direction. As the transformation occurs, the c-axis of the tetragonal pair contracts, and untransformed austenite will be placed in tension in order to maintain compatibility. This is observed as the high tensile strain near the equator in the γ austenite {200} strain pole figure. As mentioned, the lack of martensitic texture evolution suggests that transformation occurs as expansion of preexisting martensite after the build process and stress-relief heat treatment, and that no new martensite regions are nucleated. Since a large population of favorable transformation orientations already exists, the majority of the preexisting martensite readily transformed under the applied load. Importantly, this tensile loading perpendicular to the applied load implies increased stress triaxiality which is often linked to the nucleation and growth of voids. From the tomography measurements performed on the AM-SR specimen, the porosity was found to increase even at the relatively low strain levels of the test.

In addition to tensile strains perpendicular to the loading direction in the γ austenite, both the AM-SR and W specimens exhibited a large amount of strain heterogeneity in the α′ martensite perpendicular to the applied load. To more clearly show this, Fig. 11 shows variation of strain in the $\boldsymbol{e}_x^S$-$\boldsymbol{e}_z^S$ plane as a function of angle (measured counter clockwise from $\boldsymbol{e}_x^S$) in both the AM-SR (Fig. 11A) and W (Fig. 11B) specimens. In the most extreme case, {200} planes of α′ martensite in the AM-SR specimen, the strains range from close to 0 to −0.0025. As this strain variation is observed in both specimens, it is most likely related to texture rather than phase transformation. However, exact deconvolution of the effects of texture and transformation require more detailed modeling efforts. Importantly, this strain variation highlights the need to measure strains in a large number of sample directions in textured materials, such as the 17-4 specimens studied. Measurements of only one direction perpendicular to the applied load can provide misleading results that lead to incorrect conclusions about the underlying material behavior. For example, the {200} strains of the α′ martensite in the AM-SR specimen along the two transverse directions ($\boldsymbol{e}_x^S$ and $\boldsymbol{e}_z^S$) are significantly different (2.5×10^{-3} and ≈0 respectively). Some subsets of grains appear to be constrained along $\boldsymbol{e}_z^S$, which would

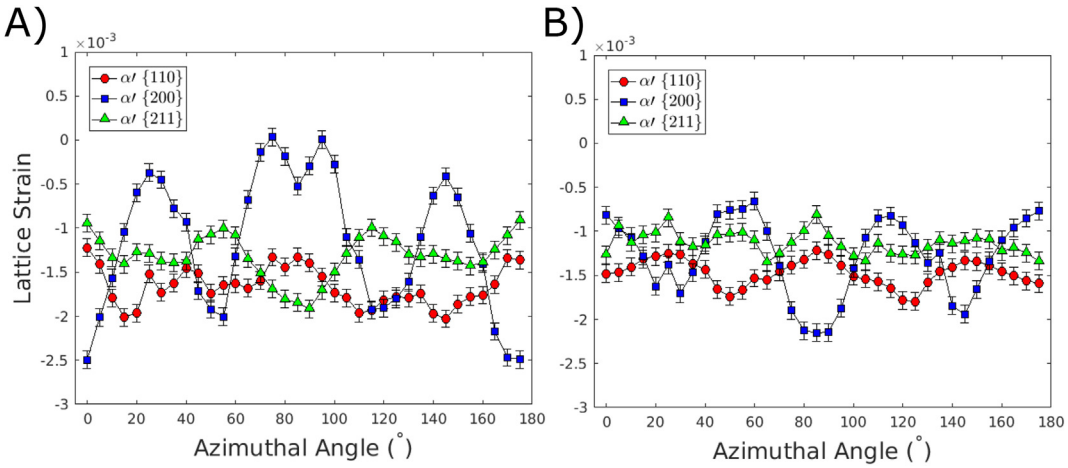

Fig. 11. Variation of lattice strains in the direction transverse to the loading direction in the α′ martensite of the A) AM-SR specimen at a macroscopic strain applied of 0.03 and B) W specimen at a macroscopic strain applied of 0.02.

be completely missed if strain measurements were performed only along $\boldsymbol{e}_{\boldsymbol{x}}^{S}$.

5. Summary

High-energy X-ray measurements were performed on additively manufactured and wrought 17-4 stainless steels *in-situ* during uniaxial deformation. From the results it was found that:

- Initial pore volume fraction of the AM-SR specimen was 1.71×10^{-4} with 125 pores identified. At the end of the test, porosity volume fraction increased slightly (by 5%) with no new pores identified. Initial pore volume fraction of the W specimen was negligible and not tracked further in the experiment.
- The martensite phase volume fraction increased from 0.46 to 0.88 after macroscopic strain of 0.03 was applied in the additively manufactured specimen, but with minimal texture evolution in both the γ austenite and α′ martensite. This behavior suggests that no new martensitic regions nucleated, and that the increase in volume fraction was primarily due to expansion of preexisting martensitic regions.
- The macroscopic stress-strain response of the AM-SR specimen was sigmoidal and similar to other works. Lattice strain data was found to be consistent with load preferentially distributing to the martensite due its higher strength.
- The strains associated with the martensitic transformation in the AM material (FCC to BCC) cause large tensile strains to develop in the austenite in lattice planes with normals near perpendicular to the applied load, suggesting high triaxiality in the untransformed austenite.
- Strong crystallographic texture in both the AM and wrought specimens is associated with significant strain heterogeneity within the same family of lattice planes. This heterogeneity demonstrates the need to measure lattice strains across a large number of sample directions in order to clearly understand the mechanical response.

Data availability

The raw data required to reproduce these findings cannot be shared at this time due to technical limitations. The processed data required to reproduce these findings are available to download from https://data.mendeley.com/datasets/3mddz99wsr/1.

Acknowledgments

This work is based upon research conducted at the Cornell High Energy Synchrotron Source (CHESS) which is supported by the National Science Foundation under award DMR-1332208.

Appendix A

This appendix provides a brief introduction to the pole figure data presented in this paper. In this work, pole figure data was determined from high-energy X-ray diffraction measurements performed in a transmission geometry (details of data processing are in §2.1). Diffraction occurs from a set of lattice planes, denoted with Miller indices *hkl*, when Bragg's law is satisfied

$$\lambda = 2d_{hkl}\sin(\theta) \tag{4}$$

where λ is the wavelength of the incoming X-ray, d_{hkl} is the lattice plane spacing, and θ is the Bragg angle. In a kinematic diffraction approximation (appropriate for metallic alloys), the intensity I_{hkl} of a diffraction event is proportional to the volume of crystal diffracting. In addition, the direction at which the diffracted X-rays are emitted $\hat{\boldsymbol{k}}_{\boldsymbol{o}}$ is related to the orientation of the normal direction $\boldsymbol{n}_{\boldsymbol{hkl}}$ of the diffracting lattice planes

$$\hat{\boldsymbol{k}}_{\boldsymbol{o}} = \hat{\boldsymbol{k}}_{\boldsymbol{i}} + \frac{\lambda}{d_{hkl}}\boldsymbol{n}_{\boldsymbol{hkl}} \tag{5}$$

where $\hat{\boldsymbol{k}}_{\boldsymbol{i}}$ is the direction of the incoming X-ray beam. By manipulating the sample orientation with respect to the incoming X-ray beam, all plane normal orientations of a family of lattice planes with respect to the sample can be probed.

As all possible lattice plane orientations with respect to an external coordinate system span the unit sphere, scalar quantities associated with the varying oriented lattice planes are naturally expressed on the same sphere. The most familiar scalar quantity is the probability *P* of finding a plane normal from the family (*hkl*) along a sample direction $\hat{\boldsymbol{q}}$ with the distribution of the probability known as an orientation pole figure. The orientation pole figure is found by noting that both the intensity of a diffraction event and the probability of finding lattice planes with normals along $\hat{\boldsymbol{q}}$ are both proportional to the volume of crystal diffracting and that the integral of the total probability distribution over the sphere must be equal to 4π [41]:

$$C\int I_{hkl}(\hat{\boldsymbol{q}})\mathrm{d}\hat{\boldsymbol{q}} = \int P_{hkl}(\hat{\boldsymbol{q}})\mathrm{d}\hat{\boldsymbol{q}} = 4\pi \tag{6}$$

where *C* is a proportionality constant. What should be taken away from the process is that a quantity associated with specifically oriented sets of lattice planes is readily mapped to the unit sphere to explore the variation as a function of orientation.

Strain pole figures can be generated and examined in a similar fashion. For a set of lattice planes with normals oriented along the direction $\hat{\boldsymbol{q}}$, their current lattice strain ε_{hkl} is defined as

$$\varepsilon_{hkl} = \frac{d_{hkl} - d_{hkl_0}}{d_{hkl_0}} = \frac{\sin(\theta_0)}{\sin(\theta)} - 1 \tag{7}$$

where 0 indicates an initial or unstrained value. From shifts in the Bragg angle, the strains of differently oriented sets of lattice planes are determined and mapped to the unit sphere in the same fashion as more traditional orientation pole figures. Importantly for interpretation, different subsets of crystals contribute to each point on the strain pole Fig. 1 a material is elastically or plastically anisotropic at the crystal scale, strain pole figures from different families of lattice planes (*hkl*) and lattice planes of varying orientation within the same family will exhibit varying mechanical responses. More information about the relationship between orientation pole figures, strain pole figures, and the underlying distributions of these quantities in orientation space is detailed in Refs. [31,42,43].

References

[1] W.E. Frazier, Metal additive manufacturing: a review, J. Mater. Eng. Perform. 23 (2014) 1917–1928.
[2] S. Lampman, T. Zorc, Properties and Selection: Irons, Steels and High Performance Alloys; Metals Handbook, ASM International, Materials Park, OH, 1990, pp. 591–592.
[3] S. Cheruvathur, E.A. Lass, C.E. Campbell, Additive manufacturing of 17-4 PH stainless steel: post-processing heat treatment to achieve uniform reproducible microstructure, JOM 68 (2016) 930–942.
[4] L.E. Murr, E. Martinez, J. Hernandez, S. Collins, K.N. Amato, S.M. Gaytan, P.W. Shindo, Microstructures and properties of 17-4 ph stainless steel fabricated by selective laser melting, J. Mater. Res. Technol. 1 (2012) 167–177.
[5] B. Clausen, D. Brown, J. Carpenter, K. Clarke, A. Clarke, S. Vogel, J. Bernardin, D. Spernjak, J. Thompson, Deformation behavior of additively manufactured gp1 stainless steel, Mater. Sci. Eng.: A 696 (2017) 331–340.
[6] G. Jacob, Prediction of Solidification Phases in Cr-Ni Stainless Steel Alloys Manufactured by Laser Based Powder Bed Fusion Process, US Department of Commerce, National Institute of Standards and Technology, 2018.
[7] D. Hackett, H. Kopech, Atomization advances in thermal spray powder, Adv. Mater. Process. 159 (2001) 31–34.
[8] S. Meredith, J. Zuback, J. Keist, T. Palmer, Impact of composition on the heat treatment response of additively manufactured 17-4 PH grade stainless steel, Mater. Sci. Eng.: A 738 (2018) 44–56.
[9] S. Mates, Private Communication, (2018).
[10] G. Janowski, F. Biancaniello, G. Hicho, R. Fields, S. Ridder, The effect of backfill and atomizing gas on the powder porosity and mechanical properties of 304 L stainless steel, P/M in Aerospace, Defense Demanding Appl. (1993) 363–370 1993.
[11] M. Averyanova, P. Bertrand, B. Verquin, Effect of initial powder properties on final microstructure and mechanical properties of parts manufactured by selective laser melting, Proceedings of the 21st International DAAAM Symposium, vol 21, 2010 No. 1.
[12] L.E. Murr, E. Martinez, K.N. Amato, S.M. Gaytan, J. Hernandez, D.A. Ramirez, P.W. Shindo, F. Medina, R.B. Wicker, Fabrication of metal and alloy components by additive manufacturing: examples of 3d materials science, J. Mater. Res. Technol. 1 (2012) 42–54.
[13] H.K. Rafi, D. Pal, N. Patil, T.L. Starr, B.E. Stucker, Microstructure and mechanical behavior of 17-4 precipitation hardenable steel processed by selective laser melting, J. Mater. Eng. Perform. 23 (2014) 4421–4428.
[14] T. Biggs, R. Knutsen, The effect of nitrogen on martensite formation in a Cr-Mn-Ni stainless steel, J. Phys. IV 5 (1995) C8–515.
[15] B.E. Warren, X-ray Diffraction, Courier Corporation, 1990.
[16] M.P. Miller, J.V. Bernier, J.-S. Park, A. Kazimirov, Experimental measurement of lattice strain pole figures using synchrotron X rays, Rev. Sci. Instrum. 76 (2005) 113903.
[17] J. Bernier, J.-S. Park, A. Pilchak, M. Glavicic, M. Miller, Measuring stress distributions in Ti-6Al-4V using synchrotron X-ray diffraction, Metall. Mater. Trans. A 39 (2008) 3120–3133.
[18] P.A. Shade, B. Blank, J.C. Schuren, T.J. Turner, P. Kenesei, K. Goetze, R.M. Suter, J.V. Bernier, S.F. Li, J. Lind, U. Lienert, J. Almer, A rotational and axial motion system load frame insert for in situ high energy x-ray studies, Rev. Sci. Instrum. 86 (2015) 093902.
[19] J. Bernier, N. Barton, U. Lienert, M. Miller, J. Strain Anal. Eng. Des. 46 (2011) 527–547.
[20] N.R. Barton, D.E. Boyce, P.R. Dawson, Pole figure inversion using finite elements over Rodrigues space, Textures Microstruct. 35 (2002) 113–144.
[21] D. Gürsoy, F. De Carlo, X. Xiao, C. Jacobsen, TomoPy: a framework for the analysis of synchrotron tomographic data, J. Synchrotron Radiat. 21 (2014) 1188–1193.
[22] V. Graphics, VG Studio Max 3.1, (2018) https://www.volumegraphics.com/.
[23] F. Kim, S. Moylan, E. Garboczi, J. Slotwinski, Investigation of pore structure in cobalt chrome additively manufactured parts using X-ray computed tomography and three-dimensional image analysis, Addit. Manuf. 17 (2017) 23–38.
[24] E. Jones, M. Iadicola, A Good Practices Guide for Digital Image Correlation, (2018) https://doi.org/10.32720/idics/gpg.ed1.
[25] W.E. Luecke, J.A. Slotwinski, Mechanical properties of austenitic stainless steel made by additive manufacturing, J. Res. Natl. Inst. Stand. Technol. 19 (2014) 398–418.
[26] J.A. Slotwinski, E.J. Garboczi, P.E. Stutzman, C.F. Ferraris, S.S. Watson, M.A. Peltz, Characterization of metal powders used for additive manufacturing, J. Res. Natl. Inst. Stand. Technol. 119 (2014) 460.
[27] H. Nyquist, Certain topics in telegraph transmission theory, Trans. Am. Inst. Electr. Eng. 47 (1928) 617–644.
[28] A.K. De, D.C. Murdock, M.C. Mataya, J.G. Speer, D.K. Matlock, Quantitative measurement of deformation-induced martensite in 304 stainless steel by X-ray diffraction, Scripta Mater. 50 (2004) 1445–1449.
[29] C. Frank, Orientation mapping: 1987 mrs fall meeting von hippel award lecture, MRS Bull. 13 (1988) 24–31.
[30] D.A. Porter, K.E. Easterling, M. Sherif, Phase Transformations in Metals and Alloys, (Revised Reprint), CRC Press, 2009.
[31] U.F. Kocks, C.N. Tomé, H.-R. Wenk, A.J. Beaudoin, Texture and Anisotropy: Preferred Orientations in Polycrystals and Their Effect on Materials Properties, Cambridge University Press, 2000.
[32] J.C. Schuren, M.P. Miller, Quantifying the uncertainty of synchrotron-based lattice strain measurements, J. Strain Anal. Eng. Des. 46 (2011) 663–681.
[33] J.C. Schuren, S.L. Wong, P.R. Dawson, M.P. Miller, Integrating experiments and simulations to estimate uncertainty in lattice strain measurements, J. Strain Anal. Eng. Des. 49 (2014) 33–50.
[34] W.F. Hosford, The Mechanics of Crystals and Textured Polycrystals, Oxford University Press, USA), 1993, p. 248 1993.
[35] S. Babu, S. Vogel, C. Garcia-Mateo, B. Clausen, L. Morales-Rivas, F. Caballero, Microstructure evolution during tensile deformation of a nanostructured bainitic steel, Scripta Mater. 69 (2013) 777–780.
[36] V. Mertinger, E. Nagy, F. Tranta, J. Slyom, Strain-induced martensitic transformation in textured austenitic stainless steels, Materials Science and Engineering: a 481-482 (2008), Proceedings of the 7th European Symposium on Martensitic Transformations, ESOMAT, 2006, pp. 718–722.
[37] P. Hilkhuijsen, H. Geijselaers, T. Bor, The influence of austenite texture on the martensitic transformation of an austenitic stainless steel, J. Alloy. Comp. 577 (2013) S609 – S613. SI :ICOMAT2011.
[38] S. Kundu, K. Hase, H. Bhadeshia, Crystallographic texture of stress-affected bainite, Proc. Math. Phys. Eng. Sci. 463 (2007) 2309–2328.
[39] P. Hedström, L.E. Lindgren, J. Almer, U. Lienert, J. Bernier, M. Terner, M. Odén, Load partitioning and strain-induced martensite formation during tensile loading of a metastable austenitic stainless steel, Metall. Mater. Trans. A 40 (2009) 1039–1048.
[40] P. Jacques, Q. Furnmont, A. Mertens, F. Delannay, On the sources of work hardening in multiphase steels assisted by transformation-induced plasticity, Philos. Mag. A 81 (2001) 1789–1812.
[41] H.J. Bunge, 4 - representation of preferred orientations, in: H.-R. Wenk (Ed.), Preferred Orientation in Deformed Metal and Rocks, Academic Press, San Diego, 1985, pp. 73–108.
[42] A. Kumar, P.R. Dawson, Modeling crystallographic texture evolution with finite elements over neo-eulerian orientation spaces, Comput. Methods Appl. Mech. Eng. 153 (1998) 259–302.
[43] H. Behnken, Strain-function method for the direct evaluation of intergranular strains and stresses, Phys. Status Solidi 177 (2000) 401–418.